


## Article

# Signatures of Pleistocene Marine Transgression Preserved in Lithified Coastal Dune Morphology of The Bahamas

Kat Wilson <sup>1,2,\*</sup>  and David Mohrig <sup>2</sup> <sup>1</sup> Department of Earth and Environmental Sciences, Boston College, Chestnut Hill, MA 02467, USA<sup>2</sup> Jackson School of Geosciences, The University of Texas at Austin, Austin, TX 78712, USA

\* Correspondence: kathleen.wilson@bc.edu

**Abstract:** The morphology of some lithified wind-blown, carbonate dunes in The Bahamas preserves the signature of erosion from paleo-marine processes: wave-induced swash, scarping, and longshore transport. Digital elevation models were used to distinguish between two dune morphotypes—those disconnected versus connected to beach processes. Dune sinuosity and upwind slope were quantified and used to interpret which dunes remained beach-attached and subject to marine erosion and processes versus dunes that became disconnected from the shoreline via inland migration or shoreline regression. Disconnected dunes possess low slopes over stoss surfaces with sinuous planforms mimicking their crestlines. Beach-connected foredunes preserve steep, kilometers-long linear upwind faces, which are interpreted to be signatures of beach-dune morphodynamics. Fore-dune morphology serves as a proxy for shoreline position during past sea-level high-stands, while the basal elevations of their stoss dune toes provide an upper limit on the beach and adjacent sea level. A growing library of digital topography will allow for this tool to be used to interpret global paleo-shoreline positions through time and space.

**Keywords:** coastal dunes; aeolianite; quaternary sea level; shallow marine carbonate sediments; The Bahamas



**Citation:** Wilson, K.; Mohrig, D. Signatures of Pleistocene Marine Transgression Preserved in Lithified Coastal Dune Morphology of The Bahamas. *Geosciences* **2023**, *13*, 367. <https://doi.org/10.3390/geosciences13120367>

Academic Editors: Giovan Peyrotty, Lucas Vimpere, Rossana Martini and Jesus Martinez-Frias

Received: 20 October 2023  
Revised: 17 November 2023  
Accepted: 25 November 2023  
Published: 28 November 2023



**Copyright:** © 2023 by the authors. Licensee MDPI, Basel, Switzerland. This article is an open access article distributed under the terms and conditions of the Creative Commons Attribution (CC BY) license (<https://creativecommons.org/licenses/by/4.0/>).

## 1. Introduction

Coastal landscapes record environmental change associated with both terrestrial and marine forcings. Within these landscapes, the form and stratigraphy of coastal dunes provide particularly valuable environmental records that include sediment supply and wind climate [1], as well as storm frequency and intensity and properties of the land surface [2–4]. Though primarily composed of beach sand, coastal dunes commonly prograde inland, driven by onshore-directed winds [5–9]. The rates and patterns of this migration can be modified by pre-existing downwind topography, vegetation, and surface moisture to the point where dunes are stabilized [10]. The sensitivity of coastal dunes to environmental boundary conditions, along with well-established classifications of dune morphology in modern coastal systems [3,4,11], suggest their form can be used to interpret both local terrestrial conditions and the extent of marine influence.

Lithified wind-blown dunes of the Quaternary age are common across The Bahamas and Turks and Caicos Islands (TCI) [6,9,12–15]. Unfortunately, connecting these dunes to contemporaneous shoreline positions remains a challenge because aeolian dunes can climb up and over pre-existing topography [16,17], potentially migrating kilometers inland without leaving a record of previous seaward positions. Finally, connecting the timing of the wind-blown sand motion and deposition with the radiometric age of the precipitation of the carbonate grain remains incompletely explored [17,18]. There is a need to identify which preserved dune forms were unambiguously connected to a paleo-shoreline versus those that are potentially disconnected by inland progradation over pre-existing topography or shoreline regression, separating them from co-incident sea level.

Carbonate landscapes offer valuable records of Pleistocene-aged coastal landforms and sedimentary facies connected to sea-level fluctuations that are less likely to be preserved in sandy, cohesionless siliciclastic systems experiencing transgression. The carbonate sediment production is limited to the shallow marine banks surrounding the islands, which forms a direct link between the source of sediment to construct aeolian dunes and sea level high-stands during the Marine Isotope Stage 5, 7, 9, and 11 interglacial periods [6,12–14,19,20]. The carbonate grains can experience rapid dissolution and diagenesis via early-stage vadose (i.e., meniscus, pendulous, and needle-fiber) cementation within tens to hundreds of years of deposition [9,21,22], increasing the preservation likelihood of the coastal dune topography. In The Bahamas and TCI, Pleistocene-aged duneforms compose most of the islands' high topography. Holocene dunes and strand plain accumulations are characteristically restricted to areas immediately adjacent to the present-day beaches [23,24]. Therefore, relict Pleistocene aeolianite geomorphology can be directly observed and interpreted from surface topography with minimal Holocene overprinting. Overall, the regional aeolian geomorphology of The Bahamas and TCI serves as a unique record of the environmental conditions, wind climate, and sea level change through the last several glacial-interglacial cycles.

The Bahamas and The Turks and Caicos archipelago (Figure 1) is composed of over 700 islands and cays sitting on carbonate banks, extending over a distance of 1000 km in a north-south direction (21° to 27° N) and at most 625 km in an east-west direction (71° 30' to 78° 50' W). The Bahamas-Caicos archipelago is entirely a carbonate province isolated from North American and Cuban terrigenous sediment input by the Florida Strait and the Old Bahamas Channel [17]. The sediment supply significant for dune development in the region is exclusively produced on the shallow (average depth = 7–10 m) marine platforms surrounding small islands during sea-level high stands. On timescales of  $10^1$ – $10^3$  years, sediments are generated through biogenic production, physiochemical precipitation (e.g., ooids and grapestones), breakdown of skeletal and reef material, tests of foraminifera, and erosion of previously deposited units or submarine cemented layers [21,25]. The characteristics of the sedimentary system mean that sediment production and availability to build aeolian dunes is directly linked with (1) relative sea level high-stands flooding the shallow platforms, (2) the construction of beaches by waves and delivery of sub-aqueous sediment, and (3) the presence of a shore platform with an elevation above mean wave height and tidal range that allows for sediment to be deposited along a beach [26,27].

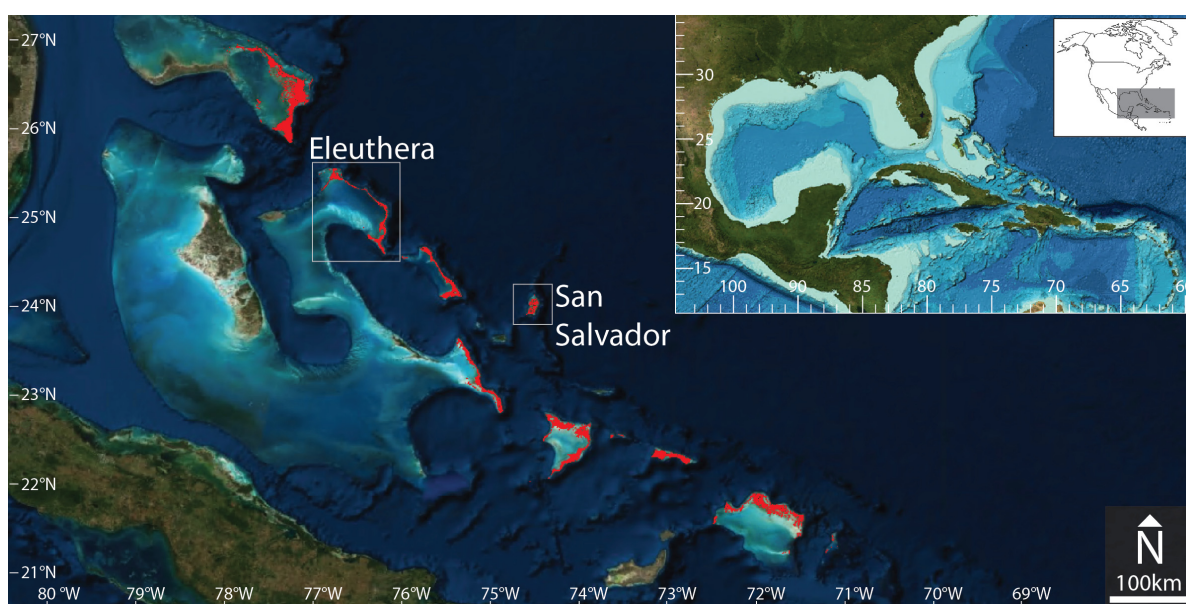


**Figure 1.** Regional map of the Bahamas and Turks and Caicos archipelago. Insets show the location of Eleuthera and San Salvador in relation to North America. The two islands featured in this study are highlighted with boxes. Modified from Rendall et al. (2022) [15].

The open Atlantic shorelines of the islands experience consistent east-west blowing easterly winds and frequent Atlantic Basin cyclonic storms. Wave energy on the Atlantic coasts is also related to the nearshore bathymetry. Narrow shelves (1–2 km) along a deep margin (e.g., 4000 m) [28] allow large (8–10 m), long-period (>10 s) open-ocean wind-driven and swell waves to attack the modern coast [29], whereas the shallow, protected banks, are characterized by tidal currents but low wave energy. Therefore, bankward sediment transport dominates due to high-energy conditions along the Atlantic coastlines and quiescent lagoon and tidal flats on the bank side.

Eleuthera (Figure 2) is a windward island, defining an approximately 130 km length of the eastern margin of Great Bahama Bank, positioned in the northern half of the archipelago (25° 33' 31" N). The sub-aerial topography of Eleuthera is dominated by sets of indurated Pleistocene aeolian dunes that reach as high as 57 m above present-day sea level (Figure 2). San Salvador (Figure 3) is a windward island that sits on a smaller bank, isolated relative to the primary trend of the archipelago. San Salvador experiences a primary wind direction from east to west; however, the wind and wave energy gradients are not as pronounced as Eleuthera because the island's western shoreline also has a steep margin and a wide zone of ocean fetch to the northwest and west. The Pleistocene ridges reach up to 42 m above present-day sea level in the interior of the island (Figure 3). In addition to the aeolianite relief, the interior of San Salvador features many lagoons, some of which are connected to marine waters via subsurface karst but have limited fetch to develop wave action. On both islands, exposure to bedrock is limited due to dense vegetative ground cover, and exposures to stratigraphy are spatially limited and randomly aligned along roadcuts. Therefore, shoreline exposures and the availability of high-resolution digital elevation models (DEMs) are particularly valuable for interpretation of the aeolian geomorphology on Eleuthera and San Salvador. Fortunately, the recent availability of high-resolution DEMs has revealed the extent, shape, and variability of dune topography, as well as signatures of past and ongoing erosion across the region. These data allow for new analysis and interpretation of coastal dune morphologies at individual duneform to island to multi-island regional scales [9,15,23], as well as other components of island geomorphology [24,30].

Digital elevation models (DEMs) of Eleuthera (Figure 2) and San Salvador (Figure 3) reveal complex aeolianite topography, which includes simple and compound dune ridges (Figure 4), sand sheets, and elongate, long-walled parabolic dunes [6,9,12,31]. Within the high-relief dune ridges (20–60 m), we observe features that are inconsistent with strictly aeolian processes: linear, upwind faces with steep (>7°) average slopes (Figure 4B,D). We hypothesize that this morphology is a signature of wave and marine processes reworking aeolian duneforms, whereas the dune ridges with sinuous, low angle (<7°) stoss slopes (Figure 4A,C) represent unmodified transverse and barchanoid aeolian depositional morphology.

Dunes shaped by aeolian processes have a characteristic asymmetrical form [32]. The maximum inclinations for stoss surfaces of aeolian dunes commonly range from 8 to 10° while lee slopes range from 20 to 30° [33,34]. The stoss sides of aeolian dunes are bounded upwind and downwind by toe-lines (Figure 4A,C) and crestlines with comparable sinuosity values [3,35]. In contrast, aeolianites with straight, steep, upwind edges resemble the morphology of beach-attached coastal foredunes, which are partially eroded by waves (i.e., dune scarping) and sculpted by longshore transport of sand [36,37]. Dune scarping occurs when waves or swash run up to and undercut the beach-adjacent dune stoss, creating a 32–90° erosional, upwind margin [38,39]. There is a net increase in the average slope and reduction in sinuosity over the foredune front relative to barchanoid and transverse dunes due to dynamic beach–dune interactions and periodic wave erosion. Wave-sculpted, beach-attached foredune morphology can be used to delineate the terrestrial limit of shoreline processes and the marine environment.

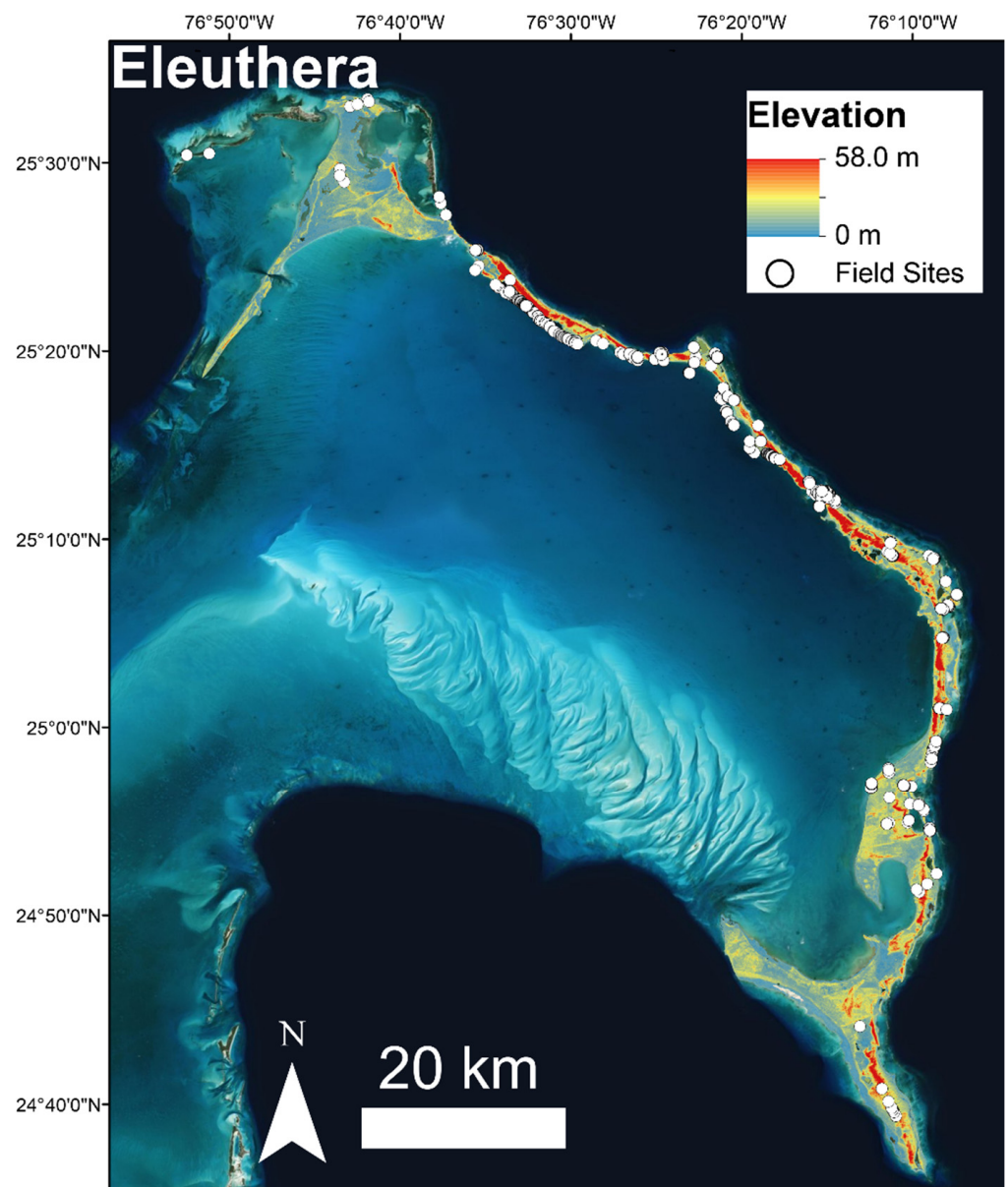


**Figure 2.** Topographic map of Eleuthera, The Bahamas, overlaid on a satellite image. The 2.5 m resolution digital surface model was acquired through the Remote Sensing Technology Center of Japan (2019). Eleuthera’s subaerial width ranges from 0.5 to 15 km, centered around  $76^{\circ}15'0''$  W. The island is roughly 136 km long, ranging from  $25^{\circ}33'31''$  N to  $24^{\circ}36'54''$  N. Locations visited by the authors between 2018 and 2021 are marked with white circles surrounded by black outlines. The prominent direction of transport and paleo-wind direction is from east to west. The shallow (<10 m) bank appears as light blue—aqua on the western, lee shadow of the island. On the east, the narrow shelf is barely visible at this scale, and the platform transitions to a deep ocean margin (>1000 m) within several km of the eastern shoreline.

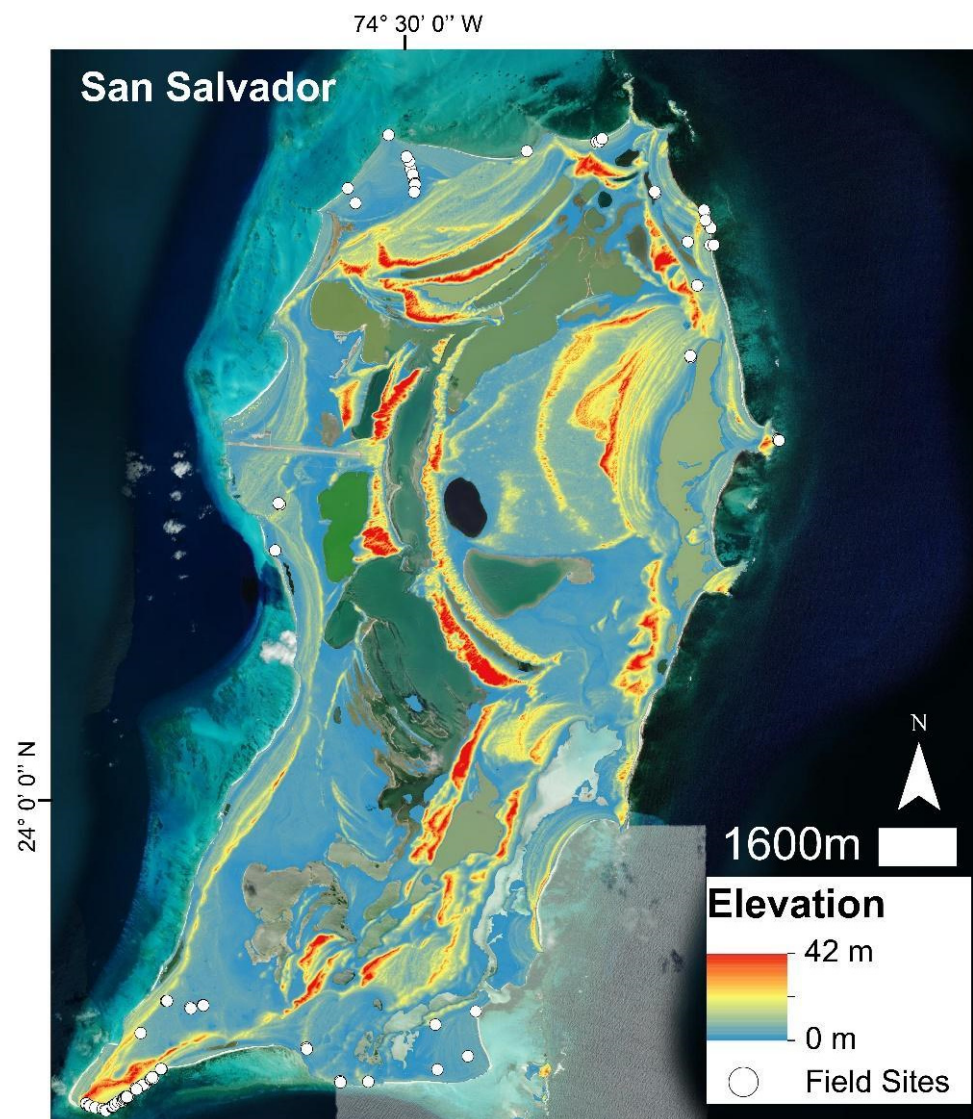


**Figure 3.** Topographic map of San Salvador Island, The Bahamas, derived from lidar, overlaid on a satellite image. The island is roughly 23 km long and 10 km wide, centered around 24°01'50'' N, 74°30'0'' W. Locations visited by the authors in 2018 are marked with white circles surrounded by black outlines. High relief areas (>7 m) are composed of aeolian units. Access and exposure of aeolianite strata is concentrated along the outer edge of the island along the coastal highway and shoreline. The prominent direction of transport and paleo-wind direction is from east to west, with some dune features showing paleo transport direction from the northeast. The shallow (<10 m) platform appears as light blue—aqua surrounding the island, and the shelf-margin transition to deep blue (>1000 m) water of the Atlantic Ocean occurs within several km of the shoreline.

The two morphological types of ridges are observed on many islands across the archipelago, suggesting the conditions producing the morphologies were regional and have environmental significance. The excellent preservation of Pleistocene aeolianites in The Bahamas allows for interrogation of their bedform sinuosity and upwind surfaces in order to distinguish the two distinct morphologic signatures of unmodified aeolian dunes and beach-attached, reworked landforms, which in turn can be used to infer the terminal paleo-shoreline position of past marine transgressions.

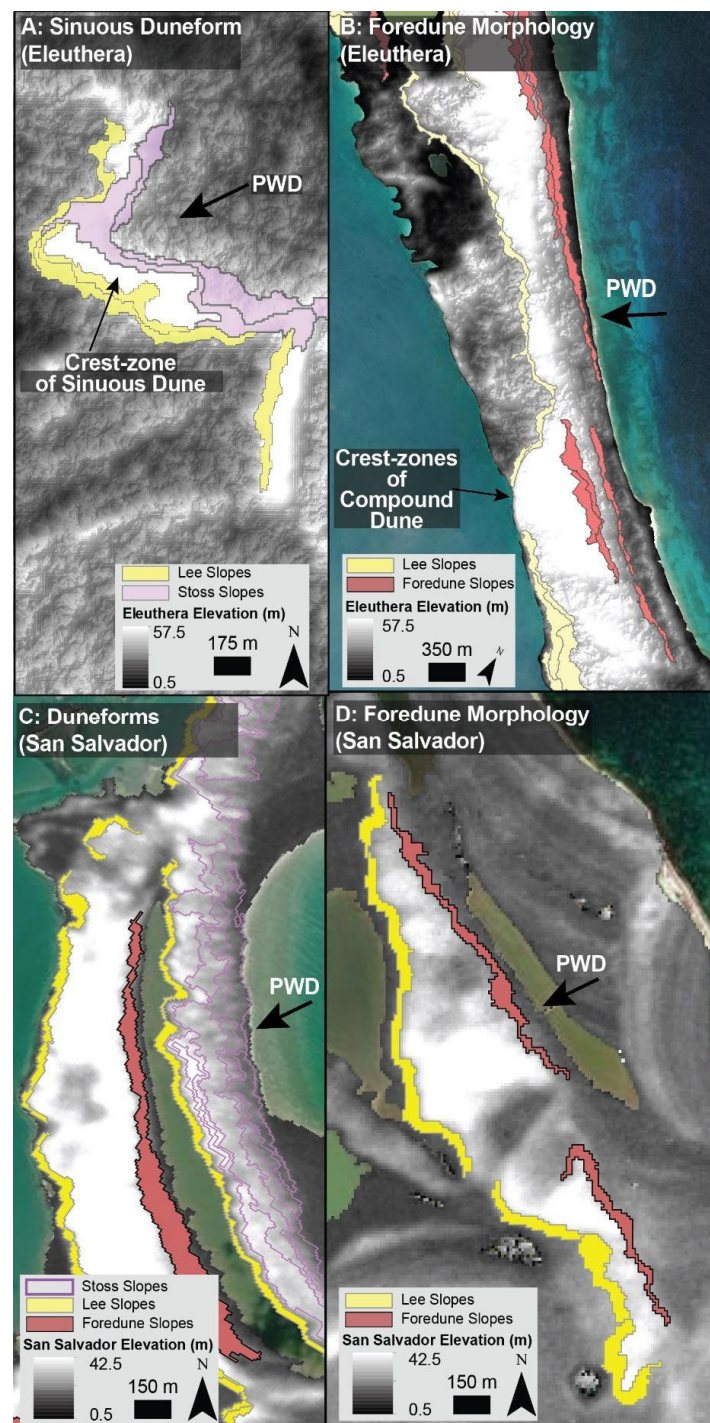


**Figure 4.** Examples of barchanoid (A) and transverse duneforms (C) and foredune morphology (B–D) from Eleuthera (A,B) and San Salvador (C,D), The Bahamas. Mapped polygons of lee, stoss, and foredune stoss slopes are shown in yellow, purple, and red. The inferred paleo-wind direction (PWD) is shown in each panel. The center point for A is  $24.936389^{\circ}$  N  $76.168889^{\circ}$  W. The center point for B is  $25.396883^{\circ}$  N,  $76.555269^{\circ}$  W. The center point for C is  $24.028611^{\circ}$  N,  $74.4875^{\circ}$  W. The center point for D is  $24.096781^{\circ}$  N,  $74.451256^{\circ}$  W.

## 2. Methods

Two topographic datasets referenced to the World Geodetic System 1984 spheroid were analyzed to identify and interpret aeolianite geomorphology. Bare-earth lidar covering San Salvador was collected by the U.S. National Center for Airborne Lidar Mapping

(NCALM) in 2016 under the permit of the Bahamian Environment Science and Technology Commission. Lidar returns were collected at a density of 16 points per square meter and gridded into 0.5 m resolution DEM. Raw data were processed by researchers at the ExxonMobil Upstream Research Company using a stationary differential base station corrected to the Continuous Operating Reference Station (CORS) network. The LiDAR DEM has a 0.2 m horizontal accuracy and an average vertical accuracy of 0.1 m [30]. A 2.5 m resolution digital surface model (AW3D) for Eleuthera covering 442 km<sup>2</sup> was acquired through the Remote Sensing Technology Center of Japan [40]. Processing was completed by RESTEC following the methods of Takaku et al. [41]. The Slope tool within ArcMap 10.8.1 was used with a 3 by 3 cell moving window to calculate the slope in degrees for each cell of the DEMs [42].

The topographic data were input to eCognition Developer, an object-based image analysis tool [43], which was used to automate the segmentation and classification of geomorphic features (Figure 5). The multi-resolution segmentation algorithm within eCognition merges cells in an optimization procedure to reduce the local heterogeneity of image objects, which in our application is a DEM. Through multiple iterations of the algorithm, neighbor cells with similar characteristics are merged to delineate the boundaries of a homogenous area until no additional best-fit mergers can be identified. Best fit grouping within the algorithm was based on characteristics of elevation above 7 m (i.e., dune ridges) (Figure 5A), average slope (Figure 5B), and slope orientation (Figure 5C). The segmentation was initiated with the default settings: scale parameter = 42; shape parameter = 0.1; compactness parameter = 0.5; export flag = 1 [44]. The eCognition approach segments components that would be mapped manually through geologic principles and intuition. However, eCognition is more efficient and systematic and can eliminate biases of manual interpretation.

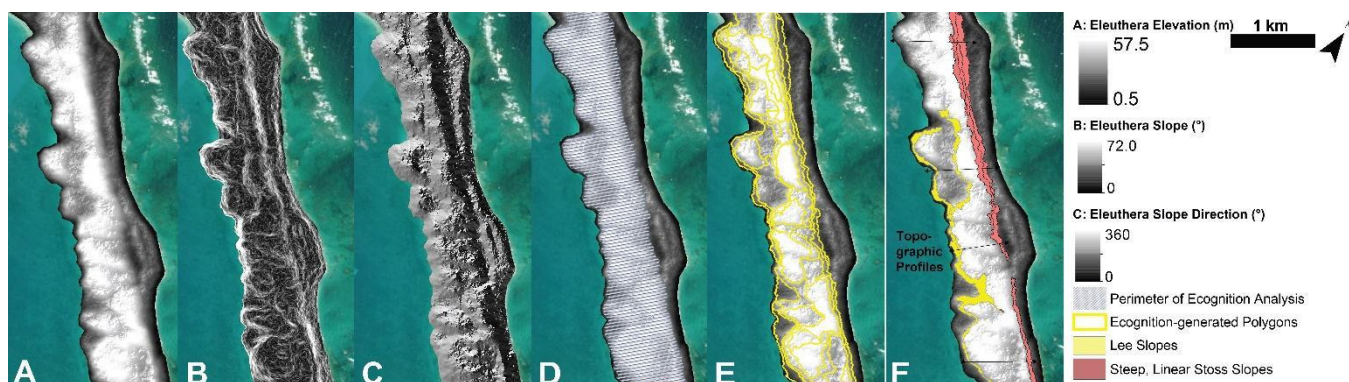


**Figure 5.** A representation of the mapping workflow in the eCognition Developer. A limited area centered on 25.24111° N, 79.288611° W is shown to highlight the detail of the mapping technique. eCognition grouped digital elevation model cells based on the similarity of elevation (A), slope (B), and slope direction (C) within the mapping perimeter (D). (E) Shows the outlines of the eCognition segmented polygons. The segmented polygons were visually interpreted as the lee slope, stoss slope, and foredune slope (F).

The segmented polygons (Figure 5E) on Eleuthera ( $n_{Ele} = 3863$ ) and San Salvador ( $n_{SS} = 2753$ ) (Table 1) were then categorized as a lee face, stoss face, and dune crest zone (Figure 5F). Polygons within 10 m of the modern shoreline were excluded from the analysis, which eliminated lithified sea cliffs and vegetated Holocene dunes (Figure 5D). Polygons associated with distinct dune ridges ( $n_{EI} = 57$ ,  $n_{SS} = 51$ ) were manually selected and merged to further reduce the number of polygons required to circumscribe each upwind ( $n_{Ele} = 229$ ,  $n_{SS} = 169$ ) and downwind ( $n_{Ele} = 153$ ,  $n_{SS} = 101$ ) face. The final polygons were used to extract the elevation and slope values from the DEMs.

**Table 1.** Summary of the number of observations from Eleuthera and San Salvador, The Bahamas.

	Number of Eleuthera Observations ( $n_{Ele}$ )	Number of San Salvador Observations ( $n_{SS}$ )
Dune ridge analyzed	57	51
Stoss face polygons	229	169
Lee face polygons	153	101
Unmodified stoss slope angle	$2.4 \times 10^6$	$4.4 \times 10^4$
Lee slope angle	$1.9 \times 10^6$	$2.0 \times 10^4$
Foredune stoss slope angle	$1.0 \times 10^6$	$7.5 \times 10^3$
Stoss and lee sinuosity (Unmodified)	32	38
Stoss and lee sinuosity (Foredune)	12	15
Slope ratio: unmodified	25	12
Slope Ratio: foredune	21	16
Dune toe elevation ( $Z_{toe}$ )	46	49

The aeolianites included in our analysis have been linked to Late Pleistocene, Marine Isotope Stage 5 (MIS 5; 80–128 ka) through stratigraphic concepts and correlation, as well as amino-acid racemization dating [12,13,18,31,45]. Through this correlation, the evaluated foredunes can be used to constrain shoreline positions and elevations associated with Pleistocene transgressions. While this contribution focuses on an interpretation of digital elevation models, field-based observations of sedimentology and stratigraphy have been fundamental to contextualizing and understanding these aeolian systems, including the interpretation of Pleistocene versus Holocene dunes from the remote sensing data. Field observations (Figures 2 and 3) were collected during three visits to Eleuthera and San Salvador, spanning 27 days between 2018 and 2021. Locations of outcrops and exposures were recorded with Google Maps or ESRI Field Maps. Additional locations were recorded using georeferenced photos taken on GPS-enabled smartphones. No physical rock or core samples were collected for this study. Aerial images were collected via a DJI Mavic Air 2 quadcopter drone.

We visually examined the final polygons for evidence of karst denudation, such as banana holes or pit caves, which, when present, can be easily identified in high-resolution DEMs [24]. However, both field-based surface observations of late Pleistocene aeolianites and remote sensing investigations indicate that karst effects are negligible within the aeolian dune polygons.

Sinuosity at the base of the stoss and lee faces was calculated on each dune by measuring the perimeter distances of the stoss and lee dune bases and then dividing by dune width, measured as the straight-line distance orthogonal to the paleo-wind direction (Figure 4). Dune stoss sinuosity (Figure 6) and stoss steepness were strongly correlated, and the parameters were used to classify the analyzed duneforms as foredune or unmodified aeolian.



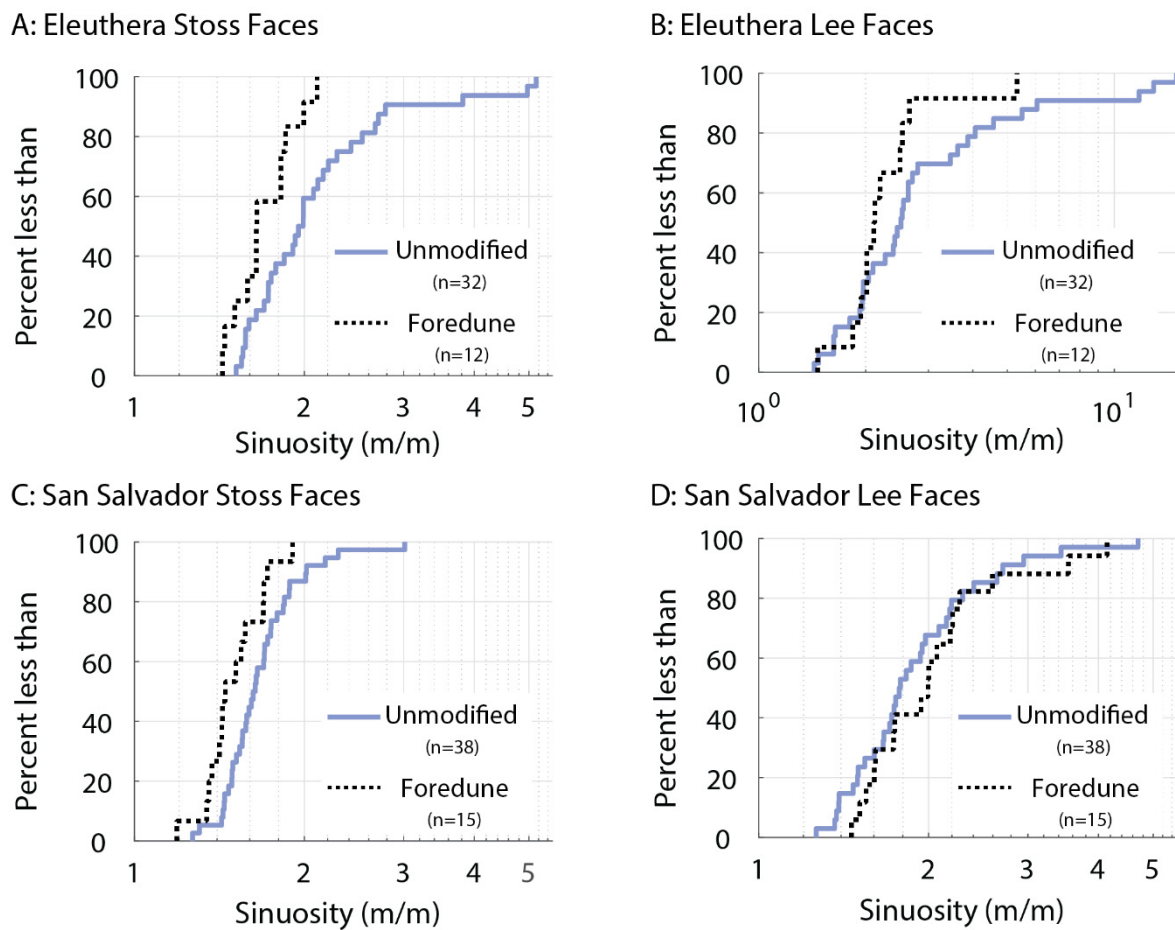


**Figure 6.** Sinuosity values for the stoss and lee face of duneforms and foredunes in Eleuthera and San Salvador. Foredunes have lower sinuosity along the stoss margin (A,C). There is no consistent pattern of differences in lee sinuosity between the two dune types (B,D).

Slope ratios ( $n = 37$ ;  $n_{\text{foredune}} = 37$ ) were calculated for paired averages of stoss and lee slope angles (Equation (1); Figure 7C), extracted from the upwind and downwind slopes of an individual dune.

$$\text{Slope Ratio} = \frac{\frac{1}{N} \sum_i^N \text{Stoss Slope}_i}{\frac{1}{M} \sum_i^M \text{Lee Slope}_i} \quad (1)$$

Topographic profiles were drawn across the aeolianites to characterize cross-sectional morphology and identify the elevation of key features. The dune toe (Figure 7A) is defined as the transition from the upper beach to the dune stoss. Dune toes are characterized as being landward of the shoreline but seaward of the dune crest and are marked by a significant local maximum in profile concavity [46]. A workflow developed to identify present-day barrier island dune characteristics [47] was adapted and used to extract dune toe elevation ( $Z_{\text{toe}}$ ) ( $n_{\text{Ele}} = 46$ ;  $n_{\text{SS}} = 49$ ) from at least two dune profiles from each foredune dune ridge, drawn parallel to the paleo-wind direction (Figure 7; Supplemental Data S3). The  $Z_{\text{toe}}$  was extracted along each profile at the largest inflection point in the slope on the stoss side of the peak dune crest elevation. On profiles without a significant change in slope, the algorithm was tuned to select the first point along the profile.

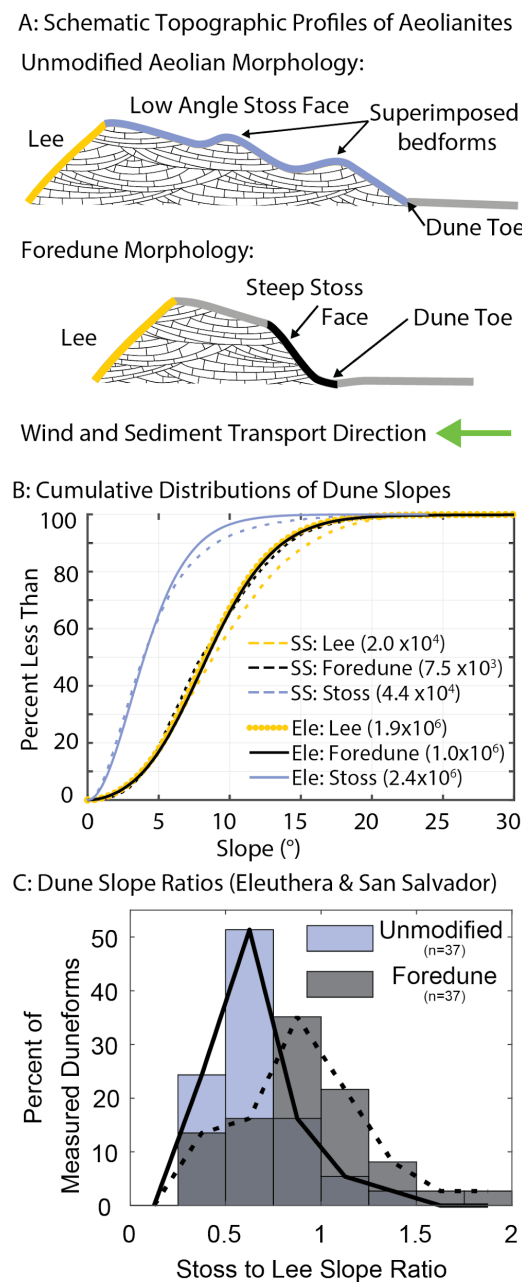


**Figure 7.** (A) Schematic topographic profiles demonstrating the geometries of transverse and barchanoid compared with foredunes. (B) Slope values for unmodified stoss, foredunes stoss, and lee faces. Foredunes on Eleuthera and San Salvador ( $\mu_{Ele} = 7.5^\circ \pm 3.7^\circ$ ;  $\mu_{SS} = 8.7^\circ \pm 4.0^\circ$ ) record the average and standard deviation values similar to lee slopes ( $\mu_{Ele} = 7.3^\circ \pm 3.8^\circ$ ;  $\mu_{Ele} = 9.3^\circ \pm 4.6^\circ$ ). Unmodified stoss faces have lower slopes ( $\mu_{Ele} = 4.5^\circ \pm 2.7^\circ$ ;  $\mu_{SS} = 4.7^\circ \pm 3.4^\circ$ ). (C) Stoss to lee slope ratios for Eleuthera and San Salvador dunes. Values close to or greater than 1 are associated with symmetrical, foredune profiles, whereas lower ratios are associated with asymmetrical aeolian-constructed topographic profiles.

### 3. Results

Unmodified duneforms on Eleuthera and San Salvador have mean stoss slopes and standard deviations of  $4.5^\circ \pm 2.7^\circ$  and  $4.7^\circ \pm 3.4^\circ$  (Figure 7B) and frequently have smaller superimposed bedforms on their stoss surfaces (Figure 7A). Stoss slopes on foredune dunes are steeper, with mean values for Eleuthera and San Salvador being  $7.5^\circ \pm 3.7$  and  $8.7^\circ \pm 4.0$  (Figure 7B). A two-sample Kolmogorov–Smirnov test determined that the unmodified and foredune stoss slopes data are not from the same continuous distribution

at a 1% significance level. In fact, the slope distributions for foredune stoss surfaces are nearly identical to the slopes of lee surfaces on the two islands (Figure 7B). As a result, foredunes are approximately symmetrical in profile (Figure 8A) and have ratios for stoss to lee slopes that are centered on 1 while values of the same ratio for unmodified dunes are mostly less than 1 (Figure 7C).

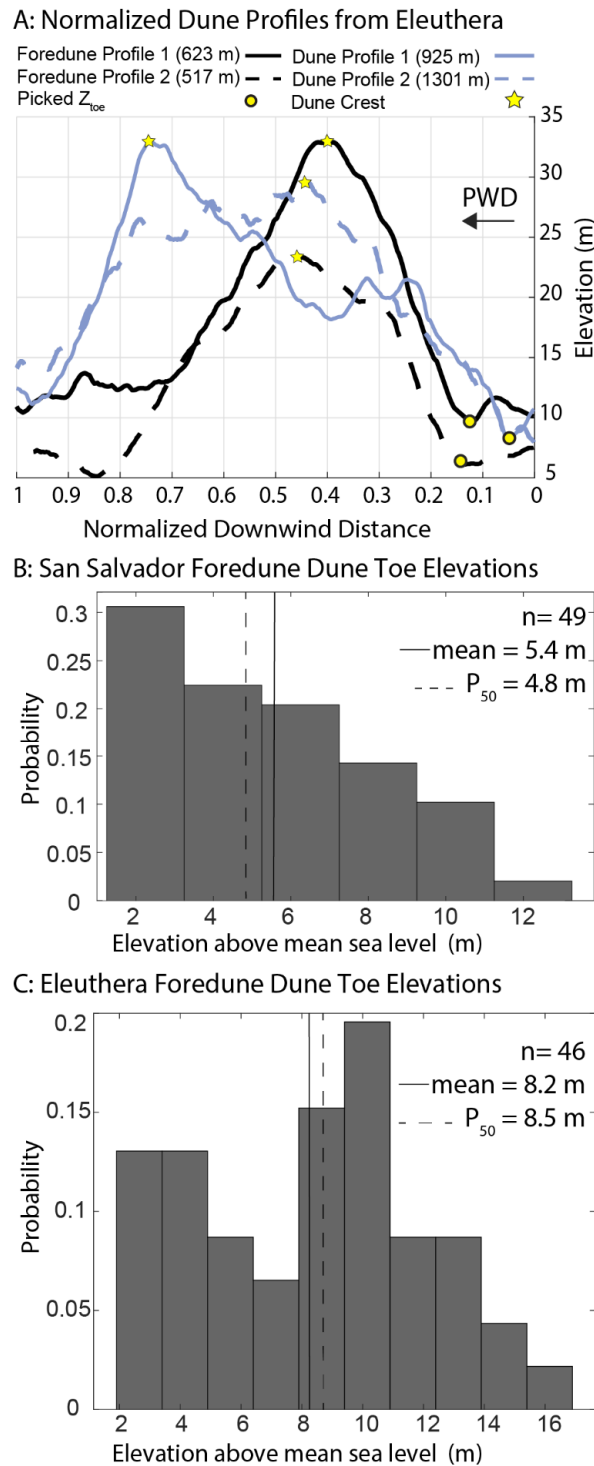


**Figure 8.** (A) Four examples of dune and foredune profiles normalized by width. The total width of each profile is reported in the legend. Dune toe elevation ( $Z_{toe}$ ) and dune crests are marked by a dot or a star. (B) San Salvador foredune  $Z_{toe}$  histogram ( $n = 49$ ;  $\mu = 5.4 \text{ m} \pm 2.9 \text{ m}$ ,  $P_{50} = 4.8 \text{ m}$ ). (C) Eleuthera foredune  $Z_{toe}$  histogram ( $n = 46$ ;  $\mu = 8.2 \text{ m} \pm 3.8 \text{ m}$ ,  $P_{50} = 4.8 \text{ m}$ ).

The stoss faces of foredunes are straighter than those found on unmodified dunes (Figure 6; Supplemental Data S1). The reduction in sinuosity is apparent in the cumulative distributions of stoss-face sinuosity that are distinct with unmodified dunes offset relative to the foredune data (Figure 6A,C). The median stoss sinuosity values for unmodified dunes on Eleuthera and San Salvador are 1.97 and 1.63, respectively. The median stoss sinuosity values for foredunes on Eleuthera and San Salvador are 1.64 and 1.45, respectively. A comparable offset is not observed in the cumulative distributions of the lee-surface sinuosity for the two dune morphotypes (Figure 6B,D). Instead, there is considerable overlap in the cumulative distributions for the lee face aeolian surfaces. On San Salvador, the lee face morphology of foredunes records greater sinuosity than the unmodified dunes.

Figure 8 shows that both the mean value and elevation range for  $Z_{toe}$  on Eleuthera ( $\mu = 8.2 \text{ m} \pm 3.7 \text{ m}$ , 1.9–16.1 m) are greater than those found on San Salvador ( $\mu = 5.4 \text{ m} \pm 2.9 \text{ m}$ , 1.3–12.6 m). In addition, the Eleuthera  $Z_{toe}$  data have a bi-modal distribution with modes at 3.4 m and 9.4 m, whereas San Salvador's data resemble a negative exponential distribution. A two-sample Kolmogorov–Smirnov test determined that the San Salvador and Eleuthera scarped  $Z_{toe}$  data are not from the same continuous distribution at a 1% significance level.

#### 4. Discussion

Field-based observations of variation in the Holocene-aged foredunes and aeolianite units (Figure 9) help inform our interpretation of the Pleistocene-aged aeolianites. The observed reductions in stoss sinuosity, combined with increases in upwind surface slopes and symmetry of cross-sectional profiles observed on the Pleistocene-aged foredunes, are consistent with morphology frequently present on beach-attached Holocene foredunes in The Bahamas.

Any dune that lies immediately adjacent to a beach can be subject to scarping and sculpting by marine processes when waves traverse the beach to interact with a dune's upwind surface. The straightening of active foredunes is a net product of continuous alongshore transport of sediment by the eroding waves. When wave impacts and marine processes are limited to collision on the dune stoss, processes affecting the morphology of lee faces are the same between foredune and non-beach attached aeolian dunes, which is consistent with similarities in slope (Figure 7B) and sinuosity (Figure 6) data.

Within active, vegetated foredunes, which may have an effective cohesion associated with pore water or an effective surface strength associated with intertwined plant roots (Figure 9A), storm waves and elevated water levels remove sediment as individual, cohesionless grains. Eroded slopes may temporarily exceed the angle of repose for sand. However, erosion by scarping steepens the stoss surface to the point where the internal angle of friction for the sand is overcome, and grain flows will redistribute sediment downslope (Figure 9A).

A second style of foredune erosion is observed in dunes with a small percentage of interparticle carbonate cement (Figure 9B). The cementation is sufficient to support small vertical cliff faces that, upon failure, immediately disintegrate into loose sand. This material collects in angle-of-repose sand piles at the base of a cliff (Figure 9B). The net result is an erosional surface that is very close in form to scarps developed in cohesionless sand. This weakly cemented sand is easily enough eroded by abrading sand grains and marine processes that at longer time scales, the topography is effectively indistinguishable from that produced of bare sand, a phenomenon that has also been observed in the gypsum sand dunes of White Sands National Park [48].

The scarping process, when the dune is composed of and breaks down into individual sand grains, produces a surface slope that is at least as steep as the friction angle,  $\sim 30^\circ$  [36]. Eroded stoss angles are considerably steeper than the original surface slopes for aeolian dune stoss that almost always range between  $0^\circ$  and  $10^\circ$  [33,34]. The stoss surfaces of loosely vegetated and weakly-cemented dunes relax into smooth, steep faces having surface slopes comparable to their lee sides. Through subsequent erosion events and stoss collapse

causing the scarp to regrade, a scarp's relief typically equals roughly the height of the foredune.



**Figure 9.** Examples of active foredune ridges (A,B) and lithified aeolianite sea cliffs (C,D) show differing styles of stoss-erosion. Active foredunes disintegrate into individual sand grains and regrade stoss angles approximately equal to the angle of repose, whereas aeolianites collapse as blocks (E) and maintain near-vertical faces, angles higher than would be observed on lee slopes.

A distinct form of dune erosion observed in Holocene dunes is associated with cemented carbonate sand that is strong enough to support vertical cliffs (Figure 9C,D). In the Bahamas, these aeolianite dunes formed in the mid-Holocene and have a greater percentage of interparticle cementation (i.e., North Point Member) [12]. Compared to cohesionless sand dunes, aeolianites exhibit properties more akin to rock, showcasing increased strength due to early diagenesis. Consequently, the erosional pattern is marked by block collapse rather than the disintegration of individual sand particles (Figure 9E). Furthermore, the erosion of the aeolianites post-cementation results in wave-cut sea cliffs that can sustain stoss angles significantly exceeding the angle of repose and the depositional angles of the lee face. On Eleuthera and San Salvador islands, the retreating aeolianite seacliffs maintain near-vertical angles, exhibit multi-meter scale surface roughness, and are associated with the widest observed wave-cut platforms (Figure 9C). These characteristics are markedly different

from active foredune morphology and the foredunes interpreted within the Pleistocene aeolianite forms.

The similarity in distributions of foredune stoss and lee slope angles for the Pleistocene aeolianites (Figure 7B) suggests that the sculpting of foredune morphology likely occurred when the now-lithified dunes were composed of loosely consolidated sand. It is interpreted that gravity-driven processes and wind-ripple reworking unconsolidated sand acted to regrade the steep lee and scarped stoss faces to the presently measured slope angles of 5–30° (Figure 7B). It would be expected that the stoss angles would be higher than the lithified lee slope angles if the stoss were eroded post-lithification into a seacliff.

Of the aeolian morphology preserved in The Bahamas, only foredunes provide an unambiguous record of the upper beach position and lateral paleo-shoreline position. Dunes that are separated from marine processes due to landward migration of the duneform or a shoreline regression are both unlikely to experience scarping on their upwind face via marine processes and cannot be confidently correlated to a paleo-shoreline position. On San Salvador, many wave-sculpted Pleistocene dunes are located in the interior of the island, providing evidence that the paleo-shoreline reached positions several kilometers (3–5 km) landward from its current position. Eleuthera foredunes indicate shorter distances of lateral translation (1–2 km) of the paleo-shoreline during past transgressions. San Salvador has a broader island width, a larger number of distinct ridges with lower maximum elevations, and more dunes that have morphologic signatures of being mobile and detached from the shoreline. Eleuthera dunes are more vertically stacked and shingled, creating a narrow, high-relief spine near the paleo-shoreline (Figure 2). Remote sensing interpretations of foredunes and associated paleo-shoreline position can be used to target locations for field-based observations and supplement in situ observations of stratigraphy and sedimentary facies. This tool provides a repeatable method and quantifiable metrics to distinguish aeolian dunes from beach-attached foredunes throughout the region and allows researchers to expand the regional understanding of the lateral position of maximum transgression.

## 5. Conclusions

The erosional surfaces on the stoss faces of coastal dunes record signatures of coastal nearshore sediment transport that can be identified through sinuosity and slope analyses. Paleo-scarped foredunes, through their connection to the upper beach, directly record the terminal position of the shoreline for any given marine transgression. The  $Z_{toe}$  for the scarped dunes on San Salvador and Eleuthera, preserves a range of elevations above present-day mean sea level (Figure 8B,C) consistent with the combined proxy and model conclusions that maximum sea level elevation during the MIS 5 was higher than today [49–52]. Additional work is needed to constrain the indicative range of the upper beach and dune toe position compared to the highest astronomical tide based on beach-dune dynamics in micro-tidal environments. However, the foredune toe can be used to demarcate the terminal position of marine influence and transition to aeolian-dominated processes.

Interestingly, the two distributions of scarped  $Z_{toe}$  on San Salvador and Eleuthera have markedly different mean and median values, as well as distribution shapes, even though the islands are separated by less than 200 km and experience similar environmental forcings such as exposure to wave and wind conditions on the windward edge of the Bahamian archipelago. Local variability in properties such as pre-existing island topography and platform geometry may have affected the timing of the production of sediment to construct dunes, which in turn may have been responsible for generating two different records of dune toe elevations and shoreline positions. The differences may also be attributed to spatial or temporal variation in mobility tied to surface properties (e.g., vegetation, moisture, and degree of cementation). Differences in glacial isostatic adjustment can vary over regional distances [53] and may also be a factor in how the two platforms and islands responded to past interglacial transgression. Therefore, the results suggest that local variability can be important in influencing the preserved paleoclimate record of marine transgression.

Initial results suggest that fossilized foredune morphology can be used elsewhere to interpret the evolution of coastal dunes, aggregate numerous shoreline data points at local and regional scales in order to adequately represent the variability in the system, and provide an additional benchmark for paleo-sea-level and glacio-isostatic adjustment models. Moreover, as the ability to radiometrically age date sand grains improves, the records of individual terminal shorelines identified by foredune dune morphologies will likely become increasingly significant. Local to regional reconstructions of shoreline position through time are important components in producing more holistic perspectives of coastal landscape evolution and will help to refine the understanding of the uncertainty throughout the course of any single sea-level cycle.

**Supplementary Materials:** The following supporting information can be downloaded at: <https://www.mdpi.com/article/10.3390/geosciences13120367/s1>, Data S1: Sinuosity Metrics and Index; Data S2: Slope Metrics and Index; Data S3: Foredune Profiles and Index.

**Author Contributions:** Conceptualization, K.W. and D.M.; methodology, K.W. and D.M.; software, K.W.; validation, K.W. and D.M.; formal analysis, K.W. and D.M.; investigation, K.W. and D.M.; resources, D.M.; data curation, K.W.; writing—original draft preparation, K.W.; writing—review and editing, K.W. and D.M.; visualization, K.W. and D.M.; supervision, D.M.; project administration, K.W. and D.M.; funding acquisition, K.W. and D.M. All authors have read and agreed to the published version of the manuscript.

**Funding:** This research received no external funding.

**Data Availability Statement:** Restrictions apply to the availability of the topographic data. Sinuosity and slope data used in this study are available in the supplementary material.

**Acknowledgments:** San Salvador lidar was collected by the National Center for Airborne Lidar Mapping under the permit of the Bahamian Environment Science and Technology Commission, funded by ExxonMobil Upstream Research Company, and shared by Jason Gulley of the University of South Florida. The purchase of Eleuthera data and supplemental visits to the Bahamas were partially funded by the Jackson School of Geosciences. Benjamin Rendall executed the ECognition algorithms. We thank Charles Kerans for logistical support during field campaigns and for many helpful discussions. The feedback from external reviewers helped to improve this manuscript.

**Conflicts of Interest:** The authors declare no conflict of interest.

## References

1. Eastwood, E.N.; Kocurek, G.; Mohrig, D.; Swanson, T. Methodology for reconstructing wind direction, wind speed and duration of wind events from aeolian cross-strata. *J. Geophys. Res. Earth Surf.* **2012**, *117*, F03035. [[CrossRef](#)]
2. Short, A.D.; Hesp, P.A. Wave, beach and dune interactions in southeastern Australia. *Mar. Geol.* **1982**, *48*, 259–284. [[CrossRef](#)]
3. Pye, K. Coastal Dunes. *Prog. Phys. Geogr.* **1983**, *7*, 531–557. [[CrossRef](#)]
4. Hesp, P.A.; Walker, I.J. 11.17 Coastal Dunes. In *Treatise on Geomorphology*; Elsevier: Amsterdam, The Netherlands, 2013; pp. 328–355. [[CrossRef](#)]
5. Pye, K. Late Quaternary Development of Coastal Parabolic Megadune Complexes in Northeastern Australia. In *Aeolian Sediments*; Pye, K., Lancaster, N., Eds.; Blackwell Publishing Ltd.: Hoboken, NJ, USA, 1993; pp. 23–44. [[CrossRef](#)]
6. Kindler, P.; Strasser, A. Palaeoclimatic Significance of co-occurring wind- and water-induced sedimentary structures in the last interglacial coastal deposits from Bermuda and the Bahamas. *Sediment. Geol.* **2000**, *131*, 1–7. [[CrossRef](#)]
7. Fornos, J.J.; Clemmensen, L.B.; Gomez-Pujol, B.L.; Murray, A.S. Late Pleistocene carbonate aeolianites on Mallorca, Western Mediterranean: A luminescence chronology. *Quat. Sci. Rev.* **2009**, *28*, 2697–2709. [[CrossRef](#)]
8. Rowe, M.P.; Bristow, C.S. Sea-level controls on carbonate beaches and coastal dunes (eolianite): Lessons from Pleistocene Bermuda. *Geol. Soc. Am. Bull.* **2015**, *127*, 1645–1665. [[CrossRef](#)]
9. Vimpere, L.; Del Piero, N.; Shawwa, N.A.; Beguelin, K.; Kindler, P.; Castelltort, S. Upper Pleistocene parabolic ridges (i.e., ‘chevrons’) from the Bahamas: Storm-wave sediments or aeolian deposits? A quantitative approach. *Sedimentology* **2021**, *68*, 1255–1288. [[CrossRef](#)]
10. Fryberger, S.G.; Krystinik, L.F.; Schenk, C.J. Tidally flooded back-barrier dunefield, Guerrero Negro area, Baja California, Mexico. *Sedimentology* **1990**, *37*, 23–43. [[CrossRef](#)]
11. Hesp, P. Foredunes and blowouts: Initiation, geomorphology and dynamics. *Geomorphology* **2002**, *48*, 245–268. [[CrossRef](#)]
12. Carew, J.L.; Mylroie, J.E. A Refined Geochronology for San Salvador Islands, Bahamas. In *Proceedings of the Third Symposium on the Geology of the Bahamas*; College Center of Finger Lakes Bahamian Field Station: Fort Lauderdale, FL, USA, 1987; pp. 35–44.

13. Hearty, P.J.; Kindler, P. The Stratigraphy and Surficial Geology of New Providence and Surrounding Islands, Bahamas. *J. Coast. Res.* **1997**, *13*, 798–812.
14. Brooke, B. The distribution of carbonate eolianite. *Earth-Sci. Rev.* **2001**, *55*, 135–164. [[CrossRef](#)]
15. Rendall, B.; Wilson, K.; Kerans, C.; Helper, M.; Mohrig, D. Coriolis effect recorded in Late Pleistocene Marine Isotope Stage 5e Bahamian aeolianites. *Geology* **2022**, *50*, 567–571. [[CrossRef](#)]
16. Vacher, H.L.; Hearty, P.J.; Rowe, M.P. Stratigraphy of Bermuda: Nomenclature, concepts, and status of multiple systems of classification. In *Terrestrial and Shallow Marine Geology of the Bahamas and Bermuda*; Curran, H.A., White, B., Eds.; Geological Society of America: Boulder, CO, USA, 1995; pp. 271–294, Geological Society of America Special Paper 300.
17. Carew, J.L.; Mylroie, J.E. Geology of The Bahamas, in Geology and Hydrogeology of Carbonate Islands. *Dev. Sedimentol.* **1997**, *54*, 91–139.
18. Hearty, P.J. Chronostratigraphy and morphological changes in Cerion land snail shells over the past 130 ka on Long Island, Bahamas. *Quat. Geochronol.* **2010**, *5*, 50–64. [[CrossRef](#)]
19. Kindler, P.; Hearty, P.J. Geology of the Bahamas: Architecture of Bahamian Islands. In *Developments in Sedimentology*; Elsevier: Amsterdam, The Netherlands, 2004; Volume 54, pp. 141–160. [[CrossRef](#)]
20. Past Interglacials Working Group of PAGES. Interglacials of the last 800,000 years Past Interglacials. *Rev. Geophys.* **2016**, *54*, 162–219. [[CrossRef](#)]
21. McKee, E.D.; Ward, W.C. Eolian. In *Carbonate Depositional Environments*; Scholle, P.A., Bebout, D.G., Moore, C.H., Eds.; American Association of Petroleum Geologists Memoir: Tulsa, OK, USA, 1983; Volume 33, pp. 131–170.
22. Caputo, M.V. Sedimentary architecture of Pleistocene eolian calcarenites, San Salvador Island, Bahamas. In *Terrestrial and Shallow Marine Geology of the Bahamas and Bermuda*; Geological Society of America: Boulder, CO, USA, 1995. [[CrossRef](#)]
23. Kerans, C.; Zahm, C.; Bachtel, S.L.; Hearty, P.; Cheng, H. Anatomy of a late Quaternary carbonate island: Constraints on timing and magnitude of sea-level fluctuations, West Caicos, Turks and Caicos Islands, BWI. *Quat. Sci. Rev.* **2019**, *205*, 193–223. [[CrossRef](#)]
24. Breithaupt, C.; Gulley, J.; Bunge, E.M.; Moore, P.J.; Kerans, C.; Fernandez-Ibanez, F.; Fullmer, S. A transient, perched aquifer model for banana hole formation: Evidence from San Salvador Island, Bahamas. *Earth Surf. Process. Landf.* **2022**, *47*, 618–638. [[CrossRef](#)]
25. Inden, R.F.; Moore, C.H. Beach Environment. In *Carbonate Depositional Environments*; Scholle, P.A., Bebout, D.G., Moore, C.H., Eds.; American Association of Petroleum Geologists Memoir: Tulsa, OK, USA, 1983; Volume 33, pp. 212–265.
26. Trenhaile, A.S. Modelling the effect of waves, weathering and beach development on shore platform development. *Earth Surf. Process. Landf.* **2005**, *30*, 613–634. [[CrossRef](#)]
27. Kennedy, D.M.; Milkins, J. The formation of beaches on shore platforms in microtidal environments. *Earth Surf. Process. Landf.* **2015**, *40*, 34–46. [[CrossRef](#)]
28. Playton, T.E.; Janson, X.; Kerans, C. Carbonate Slopes. In *Facies Models 4*; James, N.P., Dalrymple, R.W., Eds.; Geological Association of Canada: St. John's, NL, USA, 2010; pp. 449–476.
29. Wilson, K.; Mohrig, D. Modern Coastal Tempestite Deposition by a non-local storm: Swell-generated transport of sand and boulders on Eleuthera, The Bahamas. *Sedimentology* **2021**, *68*, 2043–2068. [[CrossRef](#)]
30. Breithaupt, C.I.; Gulley, J.D.; Moore, P.J.; Fullmer, S.M.; Kerans, C.; Mejia, J.Z. Flank margin caves can connect to regionally extensive touching vug networks before burial: Implications for cave formation and fluid flow. *Earth Surf. Process. Landf.* **2021**, *46*, 1458–1481. [[CrossRef](#)]
31. Hearty, P.J. The Geology of Eleuthera Island, Bahamas: A Rosetta Stone of Quaternary Stratigraphy and Sea-Level History. *Quat. Sci. Rev.* **1998**, *17*, 333–355. [[CrossRef](#)]
32. Tsoar, H. Profiles analysis of sand dunes and their steady state signification. *Geogr. Ann. Ser. A Phys. Geogr.* **1985**, *67*, 47–49. [[CrossRef](#)]
33. Sharp, R.P. Wind Ripples. *J. Geol.* **1963**, *71*, 617–636. [[CrossRef](#)]
34. Wilson, I.G. Aeolian Bedforms—Their Development and Origins. *Sedimentology* **1972**, *19*, 173–210. [[CrossRef](#)]
35. Baitis, E.; Kocurek, G.; Smith, V.; Mohrig, D.; Ewing, R.C.; Peyret, A.-P.B. Definition and origin of the dune-field pattern at White Sands, New Mexico. *Aeolian Res.* **2014**, *15*, 269–287. [[CrossRef](#)]
36. Carter, R.W.G.; Hesp, P.A.; Nordstrom, K.F. *Erosional Landforms in Coastal Dunes in Coastal Dunes Form and Process*; Nordstrom, K.F., Psuty, N., Carter, B., Eds.; John Willey & Sons: Hoboken, NJ, USA, 1990; pp. 217–250.
37. Hesp, P. *Dune Coasts, Treatise on Estuarine and Coastal Science, Volume 3*; Elsevier: Amsterdam, The Netherlands, 2011; pp. 193–221. [[CrossRef](#)]
38. Sallenger, A.H., Jr. Storm Impact Scale for Barrier Islands. *J. Coast. Res.* **2000**, *16*, 890–895.
39. Davidson, S.; Hesp, P.; Miot da Silva, G. Controls on dune scarping controls. *Prog. Phys. Geogr.* **2020**, *44*, 923–947. [[CrossRef](#)]
40. Remote Sensing Technology Center of Japan. AW3D Standard DSM. 2019. Available online: <https://www.restec.or.jp/en/index.html> (accessed on 12 December 2019).
41. Takaku, J.; Tadono, T.; Tsutsui, K.; Ichikawa, M. Validation of 'AW3D' global DSM generated from Alos Prism. *ISPRS Ann. Photogramm. Remote Sens. Spat. Inf. Sci.* **2016**, *3*, 25–31. [[CrossRef](#)]
42. Environmental Systems Research Institute Inc. *ArcGIS [GIS Software]*; Version 10.8.1; Environmental Systems Research Institute Inc: Redlands, CA, USA, 2021. Available online: <https://www.esri.com/en-us/home> (accessed on 22 February 2021).



43. Trimble, Inc. eCognition v. 10.1. 2021. Available online: <https://geospatial.trimble.com/en/products/software/trimble-ecognition> (accessed on 25 March 2021).
44. Trimble, Inc. Multi-Resolution Segmentation. 2023. Available online: <https://support.ecognition.com/hc/en-us/articles/360016173600-Multi-resolution-segmentation> (accessed on 9 October 2023).
45. Kerans, C.; Nolting, A.; Fullmer, S.; Moore, P.J.; Gulley, J.D.; Mohrig, D.C.; Hsia, S.; Wilson, K.; Breithaupt, C. *Lidar-Guided Stratigraphic Model of Pleistocene Strata, San Salvador Island, Bahamas: Sea-Level Reconstructions, Sedimentologic Models, and Carbonate Platform Development*; American Geological Union (Lecture) PP41C–1567: San Francisco, CA, USA, 2019.
46. Wernette, P.; Thompson, S.; Eyster, R.; Taylor, H.; Taube, C.; Medlin, A.; Decuir, C.; Houser, C. Defining Dunes: Evaluating How Dune Feature Definitions Affect Dune Interpretations from Remote Sensing. *J. Coast. Res.* **2018**, *34*, 1460. [[CrossRef](#)]
47. Stockdon, H.F.; Doran, K.S.; Sallenger, A.H. Extraction of Lidar-Based Dune-Crest Elevations for Use in Examining the Vulnerability of Beaches to Inundation During Hurricanes. *J. Coast. Res.* **2009**, *10053*, 59–65. [[CrossRef](#)]
48. McKee, E.D. Structures of Dunes at White Sands National Monument, New Mexico (and A Comparison with Structures of Dunes from Other Selected Areas). *Sedimentology* **1966**, *7*, 3–69. [[CrossRef](#)]
49. Kopp, R.E.; Frederik, J.S.; Mitrovica, J.X.; Maloof, A.C.; Oppenheimer, M. A probabilistic assessment of sea level variations within the last interglacial stage. *Geophys. J. Int.* **2013**, *193*, 711–716. [[CrossRef](#)]
50. Dutton, A.; Carlson, A.E.; Long, A.J.; Milne, G.A.; Clark, P.U.; DeConto, R.; Horton, B.P.; Rahmstorf, S.; Raymo, M.E. Sea-level rise due to polar ice-sheet mass loss during past warm periods. *Science* **2015**, *349*, aaa4019. [[CrossRef](#)] [[PubMed](#)]
51. Rovere, A.; Raymo, M.E.; Vacchi, M.; Lorscheid, T.; Stocchi, P.; Gómez-Pujol, L.; Harris, D.L.; Casella, E.; O’Leary, M.J.; Hearty, P.J. The analysis of Last Interglacial (MIS 5e) relative sea-level indicators: Reconstructing sea-level in a warmer world. *Earth-Sci. Rev.* **2016**, *159*, 404–427. [[CrossRef](#)]
52. Dyer, B.; Austermann, J.; D’Andrea, W.J.; Creel, R.C.; Sandstrom, M.R.; Cashman, M.; Rovere, A.; Raymo, M.E. Sea-level trends across The Bahamas constrain peak last interglacial ice melt. *Proc. Natl. Acad. Sci. USA* **2021**, *118*, e2026839118. [[CrossRef](#)]
53. Kahn, N.; Ashe, E.; Horton, B.P.; Dutton, A.; Kopp, R.E.; Brocard, G.; Engelhart, S.E.; Hill, D.F.; Peltier, W.R.; Vane, C.H.; et al. Drivers of Holocene Sea-level Change in The Caribbean. *Quat. Sci. Rev.* **2017**, *155*, 13–36. [[CrossRef](#)]

**Disclaimer/Publisher’s Note:** The statements, opinions and data contained in all publications are solely those of the individual author(s) and contributor(s) and not of MDPI and/or the editor(s). MDPI and/or the editor(s) disclaim responsibility for any injury to people or property resulting from any ideas, methods, instructions or products referred to in the content.